




# Soft cavity model for touch mechanoreceptors under static and sliding contact

P. Tapie,<sup>1</sup> D. Barreiros Scatamburlo <sup>1</sup>, A. Chateauminois <sup>2</sup>, and E. Wandersman <sup>1,\*</sup>

<sup>1</sup>*Laboratoire Jean Perrin, UMR 8237 Sorbonne Université/CNRS,*

*Institut de Biologie Paris Seine, 4 Place Jussieu, F-75005 Paris, France*

<sup>2</sup>*Laboratoire Sciences et Ingénierie de la Matière Molle, UMR 7615 CNRS, ESPCI Paris, Université PSL, Sorbonne Université, F-75005 Paris, France*



(Received 5 December 2024; accepted 15 July 2025; published 9 September 2025)

We mimic the mechanical response of touch mechanoreceptors by that of a gas cavity embedded in an elastic semicylinder, as a fingertip analog. Using tribological experiments combined with optical imaging, we measure the dynamics and deformation of the cavity as the semicylinder is put in static contact or slid against model rough surfaces at constant normal force and velocity. We propose an elastic model to predict the cavity deformation under normal load showing that membrane mechanical stresses are anisotropic and we discuss its possible biological consequences. In friction experiments, we show that the cavity shape fluctuations allow for texture discriminations.

DOI: [10.1103/ybvc-jvhn](https://doi.org/10.1103/ybvc-jvhn)

## I. INTRODUCTION

Touch mechanoreceptors are neural cells embedded in the dermis of mammals [1–3], implied in the sense of touch. In humans, the density of mechanoreceptors is particularly high around the fingertip regions and in the palm of the hand [4,5], and enables an exquisite tactile sensitivity as we explore a solid surface with our fingers, to probe its shape or roughness. Upon application of contact stresses, the skin is deformed and mechanical stresses are conveyed from the surface of the skin to the embedded mechanoreceptors, which transform mechanical signals into neural signals propagating toward the central neural system. This mechanotransduction process is performed, at the microscopic scale, by mechanosensitive transmembrane proteins (such as the Piezo protein family [6–10]) inserted in the plasmic membrane of mechanoreceptors. The structure of these mechanosensitive proteins, and as a consequence its ion permeability, depend on the membrane stresses. Under a mechanical stress, an ion flow can be triggered across the membrane, yielding to an electrical depolarization of the cell, this is the birth of an action potential.

The physiology of mechanoreceptors is well documented [2] as well as their neural response, using microneurography experiments [11,12]. In particular, two different classes of mechanoreceptors have been identified [2]: Slowly adapting (SA) mechanoreceptors on the one hand, whose neural response is triggered during the whole time duration of a mechanical stimuli and fast adapting (FA) mechanoreceptors, with a neural response that depends on the time variations of the stimuli [13]. Even if the physiology and protein sequence and structure of some mechanosensitive proteins have been recently identified, it is yet not clear to state how they precisely encode mechanical signals, and what sets microscopically peculiar dynamical responses of FA mechanoreceptors. Even

from a purely mechanical perspective, the way membrane stresses are distributed (angularly and temporarily) during a typical tactile exploration have not been measured nor modeled much.

Prior to any neural filtering, there is indeed a first purely mechanical filtering of the tactile information, performed by the geometrical and mechanical properties of the tactile organ. For instance, the presence of fingerprints (epidermal grooves with a typical wavelength  $\lambda$ ) at the extremity of the fingers modulates the subcutaneous stresses [14,15] at a temporal frequency  $v/\lambda$ , where  $v$  is the exploration velocity. In addition, the resonance properties of the skin have been shown to participate in tactile perception, by propagating mechanical stresses on large distances and thus triggering more mechanoreceptors response, even outside the finger/surface contact zone [16]. But beside these macroscopic mechanical filtering processes, one may wonder how the mechanoreceptor structure itself, as a cellular inclusion in the extracellular matrix, encode mechanical stresses; this is the purpose of this Letter.

In this work, we use a biomimetic approach and model the mechanoreceptor by a gas cavity embedded in an elastomer semicylinder, as a fingertip analog. We use optical imaging to measure the dynamics and deformation of the cavity as the finger is slid at constant velocity and normal force against a model rough surface. We discuss how the roughness of the surface is encoded in steady and fluctuating stresses at the cavity surface.

## II. ARTIFICIAL FINGER AND MECHANORECEPTOR

The biomimetic finger is an elastic semicylinder of Poly(dimethylsiloxane) (PDMS) elastomer, using a 50/50%wt mix of Sylgard 184 and Sylgard 527 (Dow Corning inc.). The mix is vigorously stirred, degassed with first a centrifugation phase (3500 rpm, 10 min) and then let in a vacuum chamber for 30 min. This liquid PDMS mixture is placed in a Plexiglas hemicylindrical mold [see Figs. 1(a1)–1(a3), inner

\*Contact author: [elie.wandersman@sorbonne-universite.fr](mailto:elie.wandersman@sorbonne-universite.fr)

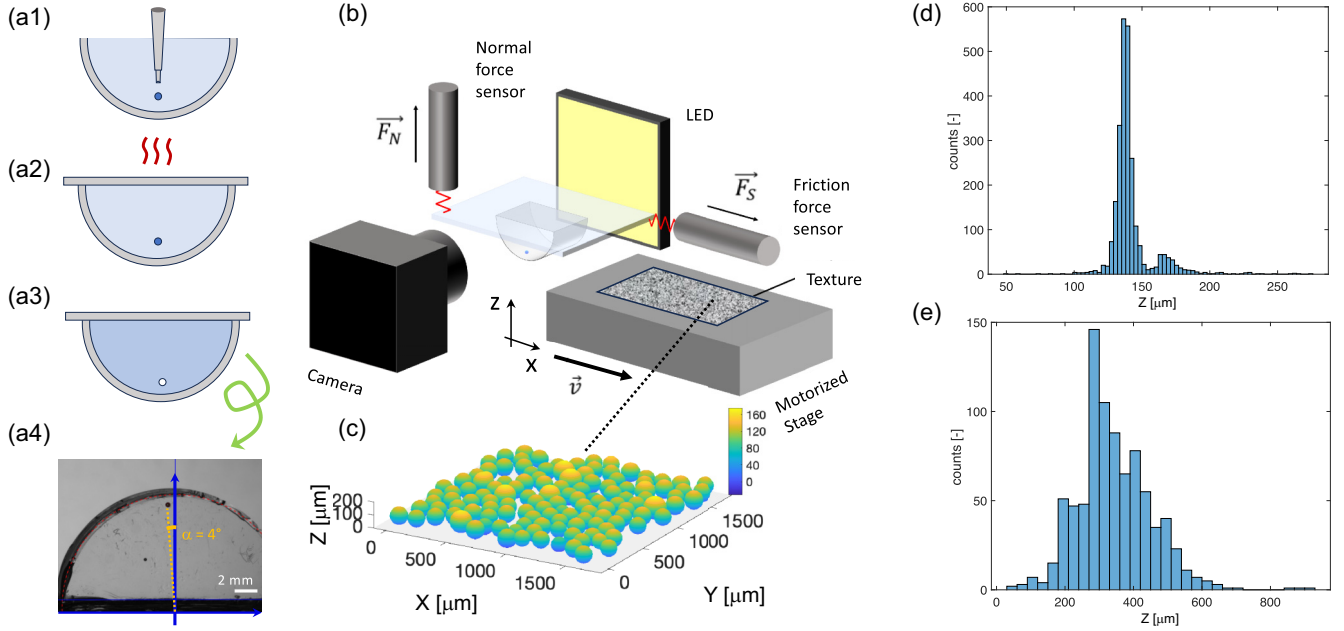


FIG. 1. (a1)–(a3) Sketch of the artificial finger/mechanoreceptor fabrication. The unreacted PDMS mix is poured in a hemicylindrical Plexiglas mold. An aqueous droplet ( $V \approx 0.5 \mu\text{L}$ ) is placed near the cylinder apex. Upon reticulation of the PDMS in an oven, the aqueous droplet evaporates and leaves a gas cavity in the elastic semicylinder. (a4) Macroscopic side-view image of the PDMS semicylinder showing the location of the cavity close to the apex. (b) Sketch of the experimental setup. (c) Z profile of the rough- surface, from profilometry measurements (see the Supplemental Material [17]). (d), (e) Histogram of the asperity heights, to which the glue base plane height has been subtracted, for the rough- (d) and the rough+ (e) samples.

radius  $R = 10 \text{ mm}$ , inner height  $h = 10 \text{ mm}$ , and length  $L = 10 \text{ mm}$ ). One droplet of deionized water (volume  $\sim 0.5 \mu\text{L}$ ) is carefully added to the mix with a micropipette, and positioned at the proximity of the cylinder apex. A plexiglas coverslip is added at the flat top of the hemicylindrical mold and the system is placed in an oven at  $65^\circ\text{C}$  for two hours for PDMS crosslinking. During crosslinking, we observed that the water of the droplet evaporates through the permeable PDMS rubber, yielding after unmolding a gas spherical cavity of radius  $a = 224 \pm 1 \mu\text{m}$  embedded in the PDMS elastomer, at a position  $z \approx 1 \text{ mm}$  from the cylinder apex [see Fig. 1(a4)]. The semicylinder rectangular base is glued to a plasma-cleaned glass plate using a few drops of PDMS which are crosslinked for a few minutes. The glass plate is then mounted on a tribological setup [see Fig. 1(b)] very similar to the one used in [15]. Briefly, the glass plate holder is mounted on two crossed dual cantilever beams (whose stiffnesses have been independently measured). The deflections of the two cantilevers are measured with two capacitive sensors, from which normal  $F_n$  and tangential forces  $F_s$  are deduced (range 0–2N), with measurement noises of about 50 mN and 10 mN, respectively. The semicylinder apex is positioned over a rough surface mounted on a manual Z translation stage (to indent the finger) and a X/Y motorized stage (ICLS-200, Newport inc.), allowing to slide the surface at constant velocity ( $v$ , from 0.05 to 0.2 mm/s). We used two different rough surfaces. The less rough one (*rough*<sup>−</sup>) is made of poly(styrene) microspheres (diameter  $d = 140 \mu\text{m}$ ) spread and glued on a microscope glass slide, the surface of which has been spin coated with epoxy glue [Fig. 1(c)]. The rougher one (*rough*<sup>+</sup>) is made using polydisperse glass microspheres ( $d =$  from 125

to  $600 \mu\text{m}$ ) glued the same way. The roughness of the rough surface is measured using an optical profilometer (Zegage Pro, Ametek inc, objective magnification  $\times 5$ ) taking images over few tens of locations in each sample (see details in the Supplemental Material [17]), from which we extract asperity height fields  $h(x, y)$ . We found, respectively, mean ( $\pm$  rms) asperity heights of  $141 \pm 16 \mu\text{m}$  for *rough*<sup>−</sup> and  $325 \pm 142 \mu\text{m}$  for *rough*<sup>+</sup> [see Figs. 1(d) and 1(e)]. Last, the cavity is imaged in transmission with a monocular zoom lens equipped with a PointGrey BlackFly S camera ( $1280 \times 1024 \text{ pix}^2$ ) with a  $\times 5$  magnification objective, yielding an image spatial resolution of  $1.7 \mu\text{m}/\text{pixel}$ . The Young's modulus  $E$  of the PDMS elastomer was measured using two methods, first by measuring the contact semiwidth  $e$  as a function of the normal force, as the finger is indented against a smooth glass surface and fitting the data with a Hertz contact model for an incompressible body [18] [ $e = \sqrt{3F_n R / (\pi L E)}$ , see Fig. 2], second by fitting linearly the normal force/indentation ( $F_n/\delta$ ) relationship (inset of Fig. 2) to an approximate solution  $F \approx \pi L E \delta / 3$  [19]. From an average of the two measurements, we obtain  $E \approx 0.8 \pm 0.2 \text{ MPa}$ , a value for PDMS mix in agreement with the results obtained in [20].

### III. RESULTS

#### A. Static contact

We first performed static contact experiments, where the apex of the finger is indented against a smooth glass plate, at constant normal force [see a sketch on Fig. 3(a)]. Using standard image analysis with a custom-made Matlab routine (see the Supplemental Material [17]) we extract the centroid

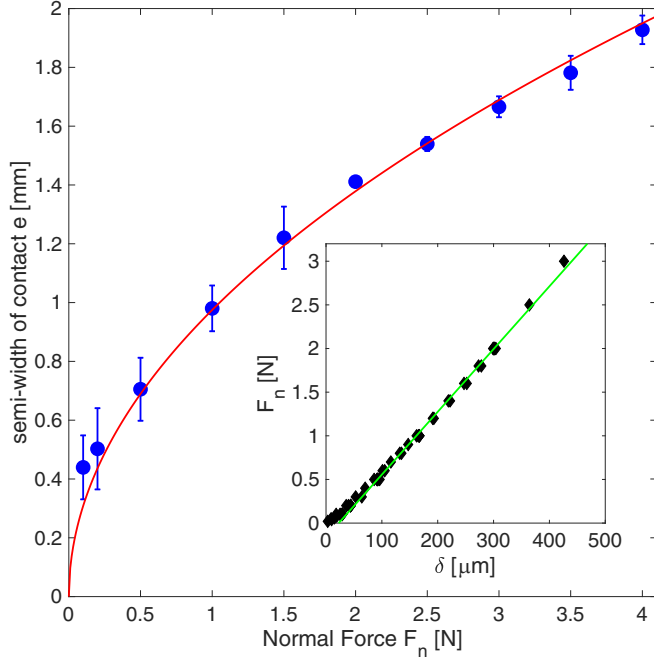


FIG. 2. Semiwidth of contact  $e$  as a function of the normal force. The solid line is a fit by a Hertz cylinder/plane model (see text). Inset: Normal force as a function of the cylinder indentation  $\delta$ . The solid line is a linear fit (see text).

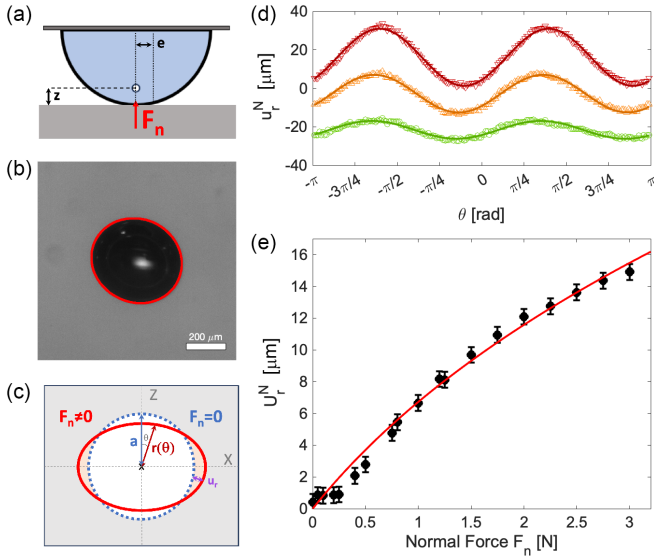


FIG. 3. (a) Sketch of the semicylinder in static normal contact with a smooth plane. (b) Image of the cavity under a  $F = 2.5$  N normal load. The detected contour has been superimposed. (c) Sketch of the undeformed (dotted line) and deformed (solid line) cavity, from which we compute the radial displacement  $u_r(\theta)$ . (d) Static radial displacement under normal load as a function of  $\theta$ , for normal force  $F_n = 0.75$  N (lower curve),  $F_n = 1.5$  N (middle curve), and  $F_n = 3$  N (upper curve). These curves have been shifted vertically arbitrarily for sake of clarity. The datas are adjusted by  $u_r = A + U_r^N \cos(2\theta + \varphi)$  (solid lines). (e) Radial displacement amplitude  $U_r^N$  as a function of the normal force. The measurement noise of  $1 \mu\text{m}$  is obtained from the standard deviation of  $U_r^N$  of repeated out-of-contact experiments. The solid line is a fit with Eq. (2).

$(x_c, z_c)$  and the contour of the cavity in polar coordinates  $r(\theta, F_n)$ , from which we deduce the static radial displacement  $u_r^N(\theta, F_n) = r(\theta, F_n) - r(\theta, F_n = 0)$  under normal load [Figs. 2(b) and (c)]. From elastic models for a cavity included in an incompressible elastic medium under a uniform compressive load [21,22], one would expect

$$u_r(\theta) \approx \frac{\sigma_0 a}{3E} \cdot \left[ \frac{3}{2} + 5 \cos(2\theta) \right]. \quad (1)$$

In the present study, the cavity is subjected to the heterogeneous stress field generated by the Hertzian cylinder-on-plane contact. However, as a first approach, we make the hypothesis that the compressive stress is homogeneous in the vicinity of the cavity and close to the value  $\sigma_0$  derived from the Hertz theory. This assumption is supported by the relatively low values of  $a/e \sim a/z \sim 0.2$ . Accordingly, the stress experienced by the cavity at a height  $z$  from the apex of the cylinder writes

$$\sigma_0 = \frac{2F_n}{\pi e L \sqrt{1 + \frac{z^2}{e^2}}}, \quad \text{yielding} \quad u_r \sim \alpha \sqrt{\frac{F_n}{1 + \frac{\beta}{F_n}}}, \quad (2)$$

where  $\alpha = 2a/3\sqrt{1/(3\pi RLE)}$  and  $\beta = z^2\pi LE/(3R)$  are two constants. The experimental measurements of  $u_r$  are well adjusted by a  $\cos(2\theta + \varphi)$  function [see Fig. 3(d)], where  $\varphi \sim \pi/8$  is a phase shift required to adjust the data, due to the fact that the cavity is not perfectly located in the contact symmetry plane [see Fig. 1(a4)]. By performing experiments in which the cavity is tilted (data not shown), we indeed found that the phase shift increases with the tilt angle. The amplitude of the  $u_r$  modulations under normal load,  $U_r^N$ , are extracted from the standard deviation of the  $u_r(\theta)$  curves, and are plotted against the normal force on Fig. 3(e). The data are reasonably well fitted with Eq. (2), with  $\alpha = 11 \pm 2 \mu\text{m}/\text{N}^{1/2}$  and  $\beta = 1.9 \pm 1 \text{ N}$ , the order of magnitude of which compares to the theoretical values  $\alpha \approx 24 \mu\text{m}/\text{N}^{1/2}$  and  $\beta = 0.8 \text{ N}$ . The cavity's response sensitivity  $\chi$  to normal indentation can be calculated from Eq. (2); it writes

$$\chi = \frac{1}{a} \left( \frac{\partial U_r^N}{\partial F_n} \right)_{F_n \rightarrow 0} = \frac{\alpha}{a\sqrt{\beta}} = \frac{2}{3\pi} \frac{1}{ELz}. \quad (3)$$

The sensitivity is expected to scale as  $1/z$  and to diverge as the cavity's location approaches the cylinder contact plane.

### B. Frictional response

Second, we performed experiments where rough surfaces are slid at a constant velocity  $v$  and constant normal force against the semicylinder [see a sketch on Fig. 4(a)], while measuring the friction force and the cavity deformations along time. We measured, at each time step in the steady sliding regime, the friction force, the centroid coordinates  $(x_c, z_c)$  of the cavity [see Fig. 4(e)] and its contour. In an attempt to isolate the shear component of the cavity deformation, we computed the radial displacement under friction force with respect to the static normal load radial profile,  $u_r^S(\theta, F_n, t) = r(\theta, F_n, F_s \neq 0) - r(\theta, F_n, F_s = 0)$  [see Fig. 4(b)]. We plot on Fig. 4(c) examples of these radial displacements under shear. Typically, the shear component induced by friction induces a sinusoidal modulation which tends to oppose to the normal

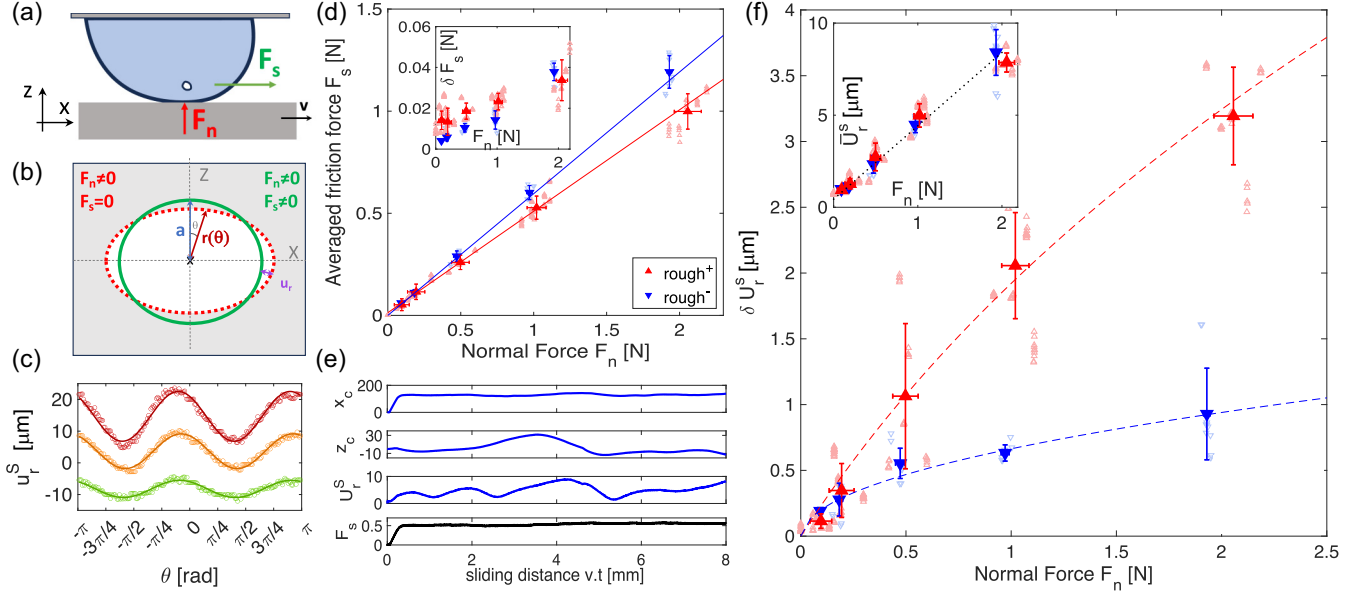


FIG. 4. (a) Sketch of the semicylinder in steady sliding against a plane rough surface, at constant velocity  $v$  and constant normal force  $F_n$ . (b) Sketch of the unsheared (dotted line) and sheared (solid line) cavity, from which the radial displacement  $u_r^s(\theta)$  is deduced. (c) Selection of radial displacement  $u_r^s(\theta)$  for the rough+ sample, at a given sliding distance ( $d = 7.33\text{ mm}$ ), and for normal forces  $F_n = 0.5\text{ N}$  (lower curve),  $F_n = 1\text{ N}$  (middle curve), and  $F_n = 2\text{ N}$  (upper curve). (d) Time averaged friction force  $\langle F_s \rangle$  as a function of the normal force for the rough+ (upward triangles) and rough- (downward triangles) rough surfaces. Inset: friction force fluctuations  $\langle \delta F_s \rangle$  as a function of  $F_n$ . The typical radial displacement amplitude  $U_r^s(t)$  at time  $t$  is obtained as  $\sqrt{2}$  times the standard deviation of  $u_r^s(\theta)$  over  $\theta$ . (e) Example of the four measured observables:  $(x_c, z_c, U_r^s, F_s)$  in  $\mu\text{m}$  and  $F_s$  in  $\text{N}$  as a function of the sliding distance for the case of the rough+ sample at  $F_n = 1\text{ N}$ . (f) Time fluctuations of  $U_r^s(t)$ , denoted  $\delta U_r^s$  as a function of  $F_n$ . The dashed lines are guides for the eyes. Inset: time averaged  $\bar{U}_r^s$  as a function of  $F_n$ .

load induced deformation, with a radial expansion at the poles and reduction at the equator. The typical amplitude of this signal  $U_r^s$  is extracted.

For these four observables  $[x_c(t), z_c(t), F_s(t), U_r^s(t)]$  we computed their time average in the steady sliding regime and their fluctuations  $(\delta x_c, \delta z_c, \delta F_s, \delta U_r^s)$ , respectively). The associated measurement noises are estimated from out-of-contact experiment (see the Supplemental Material [17]). As anticipated from the weak logarithmic dependence of the frictional stress of PDMS on velocity [23,24] in the investigated velocity range, we found that none of these observables depend on the sliding velocity in the probed range ( $v$  from 0.05 to 0.2 mm/s, see the Supplemental Material [17]), indicating that the process is quasistatic. We thus combined results at different velocities.

In Fig. 4(d) we plot the time averaged friction force as a function of the normal load, and observe a linear relationship for both roughnesses. The dynamical friction coefficient  $\mu = \bar{F}_s/F_n$  is slightly higher for the rough- texture. However, we found that the time fluctuations of the friction force  $\delta F_s$  [inset of Fig. 4(d)] are similar for both surfaces. We plot on the inset of Fig. 4(f) the time average radial displacement  $\bar{U}_r^s$  as a function of  $F_n$ . A linear relationship is obtained for both rough samples, but here again, does not allow for texture discrimination. On the contrary, we find that the time fluctuations of  $U_r^s$  are capable of discriminating textures, being threefold larger at  $F_n = 2\text{ N}$  for the rough+ sample than for the rough- one [Fig. 4(f), main pannel]. Fluctuations or other observables ( $z_c, x_c$  and  $F_n$ ) are shown in Fig. 6 and discussed in the Appendix below.

#### IV. DISCUSSION

Altogether, this work proposes a mechanical framework to predict the elastic part of mechanoreceptor deformations upon stereotypical tactile tasks. Is this simplified model applicable to natural mechanoreceptors?

Natural mechanoreceptors are of various types and sizes [2]: Merkel cells for instance are typically  $\sim 10\text{ }\mu\text{m}$  in diameter, while Pacinian corpuscles can reach  $100\text{ }\mu\text{m}$ – $1\text{ mm}$  [25,26]. The latter are thus comparable in size to our model cavity (diameter  $\sim 400\text{ }\mu\text{m}$ ). In addition, these receptors are typically located at depths of approximately hundreds of  $\mu\text{m}$  to 2 mm beneath the skin surface—also comparable to our model configuration.

The typical membrane tensions  $\gamma$  of eukaryotes cell typically lie around  $10^{-2}$  to  $1\text{ mN/m}$  scale [27,28]. Taking a typical value of  $E = 100\text{ kPa}$  for the Young's modulus of the human finger [29], one obtains an elastocapillary length [30]  $l_{ec} = \gamma/E < 10\text{ nm}$ , which is extremely small with respect to the mechanoreceptor diameter. This suggests that elastic stresses are the dominant contribution in predicting mechanoreceptor deformations, and cell surface tension can be neglected at this scale.

Natural mechanoreceptors, however, embed a complex biological aqueous content within a plasma membrane composed of a lipid bilayer with various embedded proteins, and are surrounded by a viscoelastic extracellular matrix. To approach this complexity, we previously developed lipid vesicle-like systems embedded in a hydrogel. In a recent paper [31], we demonstrated how to create and trap a lipid

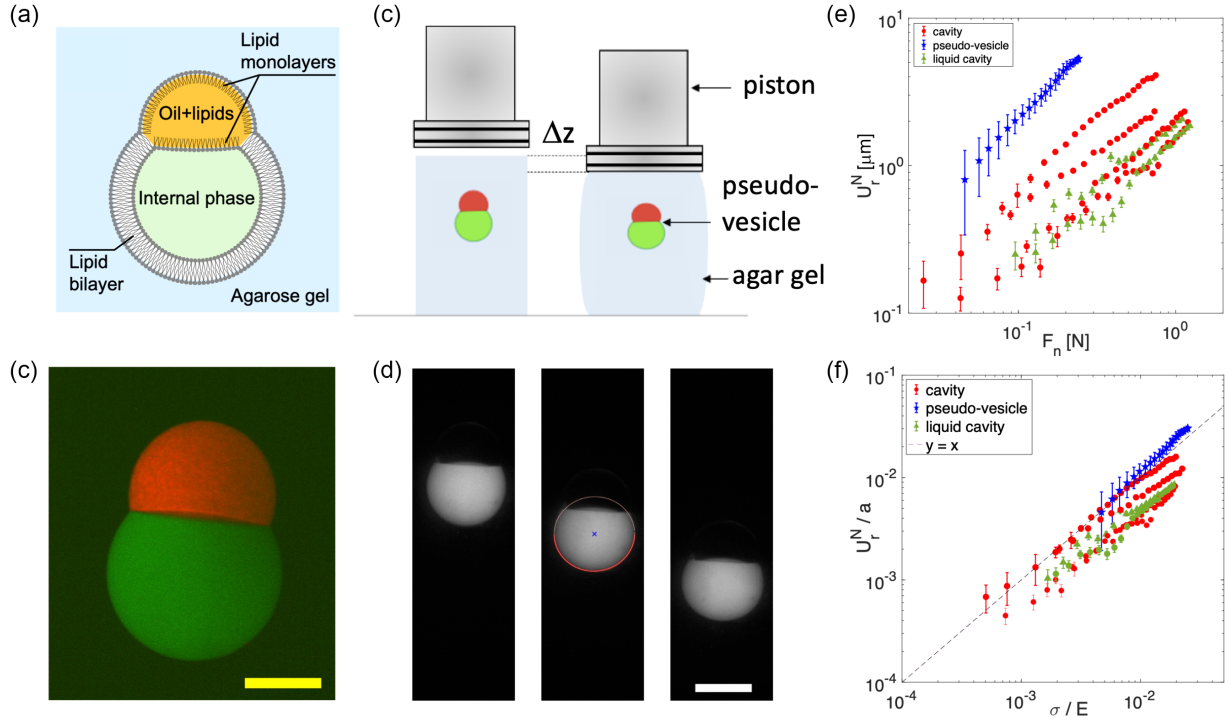


FIG. 5. See also [31]. (a) Sketch of a pseudovesicle trapped in an agar gel. (b) Fluorescence image of the pseudovesicle, whose internal aqueous phase is marked with a green fluorophore and the oil phase in red (scale bar 200 μm). (c) Sketch of the plane/plane deformation setup. (d) Fluorescence images of the pseudovesicle upon deformation. The scale bar is 400 μm long. (e) Radial deformation  $U_r^N$  as a function of the normal force, for gas cavities (red discs) a liquid cavities (green triangles) and pseudovesicle (blue stars). (f) Rescaled  $U_r^N/a$  as a function of rescaled stress  $\sigma/E$ .

pseudovesicle within an aqueous agar gel. The term pseudovesicle refers to a lipid vesicle with an oily cap on top [Figs. 5(a) and 5(b)]. The agar gel (Young's modulus  $E \sim 100$  kPa) can be indented using a piston with a cross-sectional area  $S$  [Figs. 5(c) and 5(d)], and its deformation  $u_r^N$  can be measured under a normal load in a plane-plane contact. In the Supplemental Material of [31], we showed that the deformation of the pseudovesicle closely approximates that of a gas cavity in a PDMS elastomer, as studied in the present work. Notably, when the deformation  $U_r^N$  is rescaled by the radius  $a$  of the pseudovesicle (or cavity), and the applied compressive stress  $\sigma = F_n/S$  is normalized by the Young's modulus  $E$ , the curves for different systems collapse onto a single trend [Figs. 5(e) and 5(f)]. These results support the relevance of our gas cavity model as a first-order approximation to describe mechanoreceptor deformation, even in more biologically realistic contexts.

Using this elastic model under static normal load, we can estimate the order of magnitude of the strain at the cavity wall as  $\epsilon \approx \ln(1 + U_r/a) \approx 0.02$ . This corresponds to a stress  $\sigma_{\theta\theta} \sim E u_r^N/a \sim \sigma_0$  of the order of 10 kPa. For biological mechanoreceptors, how much does the membrane tension  $\Delta\gamma$  increase upon contact? This can be estimated using the typical area expansion modulus  $K \sim 100$  mN/m of a cell membrane [32,33]:  $\Delta\gamma = K \frac{\Delta A}{A}$ , with  $A$  the membrane area. One can estimate  $\Delta\gamma \sim K U_r^2/a^2 \sim K (\frac{\sigma_0}{E})^2$ , leading to  $\Delta\gamma \sim 1$  mN/m—within the range of threshold tensions required to activate mechanosensitive proteins [6,10].

Using this elastic model, we also found that the static contact sensitivity  $\chi$  increases and diverges as the cavity approaches the cylinder apex [Eq. (3)]. However, from a biological perspective, a balance is likely required between tactile sensitivity and structural integrity. Merkel corpuscles—specialized touch mechanoreceptors for static contact—are located approximately 1 mm beneath the skin, within dermal papillae [1], just below the epidermis, which may act as a protective layer.

Second, from Eq. (2), the anisotropic experimental radial displacement  $U_r^N$  leads to an anisotropic hoop stress  $\sigma_{\theta\theta}$ : compressive at the cavity equator and extensional at the poles. This anisotropy is well known in geophysics to explain fracture localization in pressurized rock cavities [34,35], but has not been considered in the context of tactile perception. This suggests that mechanosensitive proteins may have different activation probabilities depending on their angular location. Could protein distribution be anisotropic, e.g., concentrated at the poles to enhance sensitivity? Alternatively, the density may adapt dynamically to membrane curvature, via a negative curvotaxislike mechanism, as observed for various membrane proteins [36–39].

Finally, regarding texture discrimination, our findings suggest that shape fluctuations—and consequently, stress fluctuations—enable roughness detection of textured surfaces. This calls for mechanical models of cavities under tangential/frictional forces. A first step is presented in the Supplemental Material [17], where we analyze the cavity response

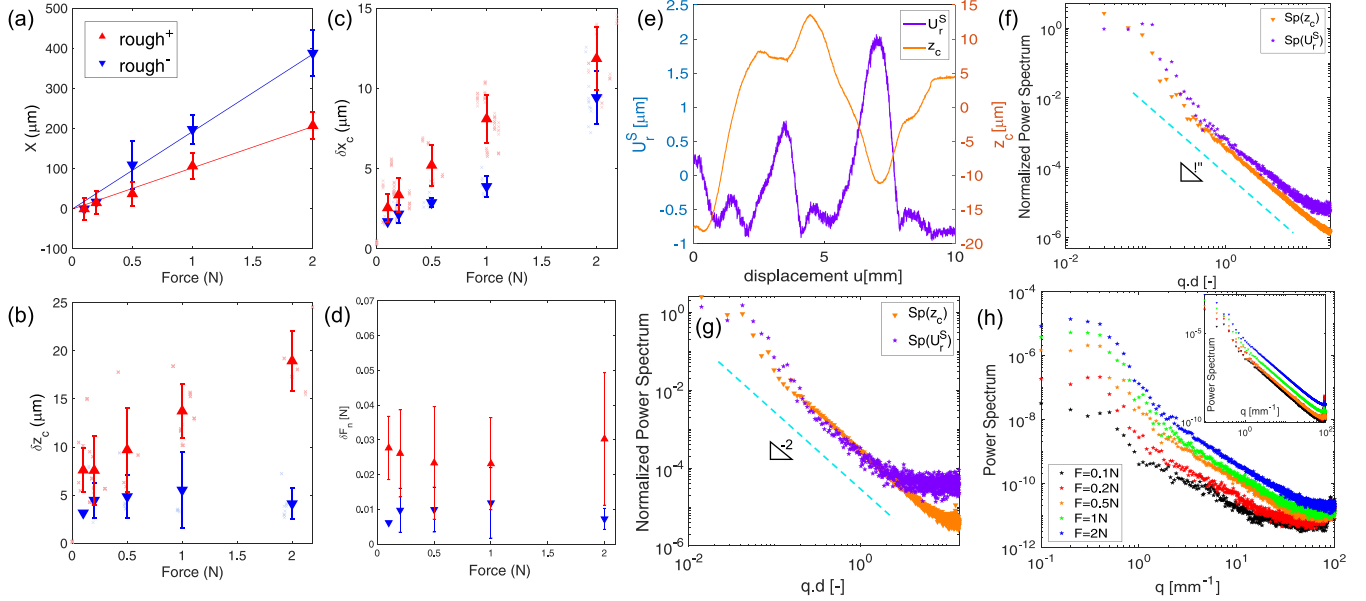


FIG. 6. (a) Time-averaged  $x_c$  displacement of the cavity centroid,  $X$ , as a function of the normal load. The lines are linear fits to the data. (b) Standard deviation of  $z_c$  displacement,  $\delta z_c$ . (c) Standard deviation of  $x_c$  displacement,  $\delta x_c$ . (d) Normal force fluctuation  $\delta F_n$  as a function of the normal load. (e) Time traces of the  $z_c$  displacement (orange, right scale) and  $U_r^S$  (purple, left scale). The signal averages have been subtracted. (f) Normalized power spectrum of  $z_c$  and  $U_r^S$  as a function of the normalized wave vector  $q.d$ ,  $d$  being the averaged particle diameter, for the rough+ sample, at  $F_n=0.5$  N. (g) Same for the rough- sample. (h) Power spectrum of the deformation  $U_r^S$  for different normal load, for rough+ sample. Inset: spectrum of  $z_c$ .

to the passage of a single surface defect. From a biological perspective, this gives a mechanical rationale for the existence of fast adapting mechanoreceptors, whose neural response is tuned to stress fluctuations.

#### APPENDIX: FLUCTUATIONS AND POWER SPECTRUMS

In Figs. 6(a) and 6(c) we have plotted the average and standard deviation of the  $x_c$  position as a function of the normal load, for both textures. We observe that the time-averaged  $\bar{x}_c$  increase quasilinearly with the normal force, with a slope, respectively, of  $380 \mu\text{m}/\text{N}$  (resp.  $205 \mu\text{m}/\text{N}$ ) for the rough- (rough+) surface, allowing to discriminate both textures. Noticeably, the magnitude of the time averaged lateral displacement  $x_c$  of the cavity is correlated to the magnitude of the friction forces reported in Fig. 4(d). Conversely, the fluctuations of  $x_c$  on the contrary are not good texture discriminants. In the transverse  $Z$  direction, fluctuations  $\delta z_c$  are separated for rough- and rough+ samples. Typically, values of  $\delta z_c$  are larger in amplitude than  $\delta U_r^S$  fluctuations [Fig. 4(f)] but increase more moderately with the normal load. Finally, let

us note that the normal force fluctuations are not statistically different for the different textures [Fig. 6(d)].

What are the differences between the  $\delta z_c$  and the  $\delta U_r^S$  fluctuations? In Fig. 6(e) we plot time traces of  $z_c(v.t)$  and  $U_r^S(v.t)$ . Typically, the  $z_c$  signal shows more large wavelength fluctuations than  $\delta U_r^S$ . This can be better evidenced by looking at the power spectrum of  $z_c$  and  $U_r^S$  fluctuations, as plotted in Figs. 6(f) (rough+) and 6(g) (rough-), as a function of the normalized wave vector  $q.d$ ,  $d$  being the particle diameter. Note that these spectrum have been normalized by the variance of the corresponding signal, to cancel their amplitude differences. The  $z_c$  spectrum are found to decay as  $q^{-2}$  over the whole wave vector range. The  $U_r^S$  spectrum is quite comparable at low wave vectors, but present an excess of noise density at larger wave vectors, with a crossover at  $q.d \sim 1$ . It suggests that shape fluctuations are more sensitive to shorter length scale, close to the particle roughness length scale. We also found that the shape fluctuation spectrum is more sensitive to normal force variations than position fluctuations [Fig. 6(h)], since different spectra at different normal forces are more separated.

[1] D. Deflorio, M. Di Luca, and A. M. Wing, *Front. Hum. Neurosci.* **16**, 862344 (2022).  
 [2] A. Handler and D. D. Ginty, *Nat. Rev. Neurosci.* **22**, 521 (2021).  
 [3] R. S. Johansson and A. B. Vallbo, *J. Physiol.* **286**, 283 (1979).  
 [4] R. S. Johansson and Å. B. Vallbo, *Trends Neurosci.* **6**, 27 (1983).

[5] A. B. Vallbo, R. S. Johansson *et al.*, *Hum neurobiol.* **3**, 3 (1984).  
 [6] S. S. Ranade, S.-H. Woo, A. E. Dubin, R. A. Moshourab, C. Wetzel, M. Petrus, J. Mathur, V. Bégay, B. Coste, J. Mainquist *et al.*, *Nature (London)* **516**, 121 (2014).  
 [7] S.-H. Woo, S. Ranade, A. D. Weyer, A. E. Dubin, Y. Baba, Z. Qiu, M. Petrus, T. Miyamoto, K. Reddy, E. A. Lumpkin *et al.*, *Nature (London)* **509**, 622 (2014).

- [8] Q. Zhao, H. Zhou, S. Chi, Y. Wang, J. Wang, J. Geng, K. Wu, W. Liu, T. Zhang, M.-Q. Dong *et al.*, *Nature (London)* **554**, 487 (2018).
- [9] L. Wang, H. Zhou, M. Zhang, W. Liu, T. Deng, Q. Zhao, Y. Li, J. Lei, X. Li, and B. Xiao, *Nature (London)* **573**, 225 (2019).
- [10] P. Delmas, T. Parpaite, and B. Coste, *Neuron* **110**, 2713 (2022).
- [11] M. Knibestöl and Å. B. Vallbo, *Acta Physiologica Scandinavica* **80**, 178 (1970).
- [12] R. Johansson, in *Sensory Functions of the Skin in Primates* (Elsevier, 1976), pp. 159–170.
- [13] S. J. Bolanowski Jr, G. A. Gescheider, R. T. Verrillo, and C. M. Checkosky, *J. Acoust. Soc. Am.* **84**, 1680 (1988).
- [14] J. Scheibert, S. Leurent, A. Prevost, and G. Debrégeas, *Science* **323**, 1503 (2009).
- [15] E. Wandersman, R. Candelier, G. Debrégeas, and A. Prevost, *Phys. Rev. Lett.* **107**, 164301 (2011).
- [16] L. R. Manfredi, A. T. Baker, D. O. Elias, J. F. Dammann III, M. C. Zielinski, V. S. Polashock, and S. J. Bensmaia, *PLoS ONE* **7**, e31203 (2012).
- [17] See Supplemental Material at <http://link.aps.org/supplemental/10.1103/ybvc-jvhn> for some details on the experimental system and methods.
- [18] K. L. Johnson and K. L. Johnson, *Contact Mechanics* (Cambridge University Press, Cambridge, 1987).
- [19] V. L. Popov *et al.*, *Contact Mechanics and Friction* (Springer Berlin, Heidelberg, 2010), pp. 231–253.
- [20] R. N. Palchesko, L. Zhang, Y. Sun, and A. W. Feinberg, *PLoS ONE* **7**, e51499 (2012).
- [21] J. C. Jaeger, N. G. Cook, and R. Zimmerman, *Fundamentals of Rock Mechanics* (John Wiley & Sons, Oxford, 2009).
- [22] I. S. Sokolnikoff, *Mathematical Theory of Elasticity*, Vol. 49 (McGraw-Hill Book Company. Inc., New York, London, 1956), pp. 51–52.
- [23] D. T. Nguyen, S. Ramakrishna, C. Frétiigny, Y. Le Chenadec, and A. Chateauminois, *Tribol. Lett.* **49**, 135 (2013).
- [24] V. Fazio, V. Acito, F. Amiot, C. Frétiigny, and A. Chateauminois, *Proc. R. Soc. A* **477**, 20210559 (2021).
- [25] J. Bell, S. Bolanowski, and M. H. Holmes, The structure and function of pacinian corpuscles: A review, *Prog. Neurobiol.* **42**, 79 (1994).
- [26] D. C. Pease and T. A. Quilliam, Electron microscopy of the pacinian corpuscle, *J. Biophys.* **3**, 331 (1957).
- [27] M. M. Kozlov and L. V. Chernomordik, Membrane tension and membrane fusion, *Curr. Opin. Struct. Biol.* **33**, 61 (2015).
- [28] E. Fischer-Friedrich, A. A. Hyman, F. Jülicher, D. J. Müller, and J. Helenius, Quantification of surface tension and internal pressure generated by single mitotic cells, *Sci. Rep.* **4**, 6213 (2014).
- [29] C. Opreșan, V. Cârlescu, A. Barnea, G. Prisacaru, D. Olaru, and G. Plesu, in *IOP Conference Series: Materials Science and Engineering*, Vol. 147 (IOP Publishing, 2016), p. 012058.
- [30] R. W. Style, R. Boltyanskiy, B. Allen, K. E. Jensen, H. P. Foote, J. S. Wettlaufer, and E. R. Dufresne, *Nat. Phys.* **11**, 82 (2015).
- [31] P. Tapie, A. M. Prevost, L. Montel, L.-L. Pontani, and E. Wandersman, *Sci. Rep.* **13**, 5375 (2023).
- [32] J. S. Najem, M. D. Dunlap, I. D. Rowe, E. C. Freeman, J. W. Grant, S. Sukharev, and D. J. Leo, *Sci. Rep.* **5**, 13726 (2015).
- [33] A. S. Reddy, D. T. Warshaviak, and M. Chachisvilis, *Biochim Biophys Acta Gen Subj.* **1818**, 2271 (2012).
- [34] E. Lajtai, *Tectonophysics* **11**, 129 (1971).
- [35] T. Davis, D. Healy, A. Bubeck, and R. Walker, *J. Struct. Geol.* **102**, 193 (2017).
- [36] C. Has and S. L. Das, *Biochim Biophys Acta Gen Subj.* **1865**, 129971 (2021).
- [37] D. H. Johnson, O. H. Kou, N. Bouzos, and W. F. Zeno, *Trends Biochem. Sci.* **49**, 401 (2024).
- [38] B. Sorre, A. Callan-Jones, J. Manzi, B. Goud, J. Prost, P. Bassereau, and A. Roux, *Proc. Natl. Acad. Sci. USA* **109**, 173 (2012).
- [39] C. Prévost, H. Zhao, J. Manzi, E. Lemichez, P. Lappalainen, A. Callan-Jones, and P. Bassereau, *Nat. Commun.* **6**, 8529 (2015).